# Detection of artificially injected signals in the cosmic microwave background

Sophie Zhang[*]
*Department of Physics, University of Michigan,*
*450 Church St, Ann Arbor, MI 48109-1040*

Advisor: Professor Dragan Huterer[†]
*Department of Physics, University of Michigan,*
*450 Church St, Ann Arbor, MI 48109-1040*

**Background and purpose:** One of the triumphs of modern cosmology has been the detection and measurement of anisotropies in the cosmic microwave background (CMB), thermal radiation left over from the Big Bang. Though almost completely uniform, it contains inhomogeneities on the order of $10^{-5}$, one part in $100,000$, imparting important information regarding the nature of our universe.

One of the questions cosmologists today must consider is if our standard cosmological model is an accurate description of the universe, or if pieces are missing. Detection of anomalies, such as odd alignments in multipole vectors or unusually hot/cold regions of the sky, could provide evidence for missing pieces in our understanding of the universe. However, in order to detect such anomalies, one must first devise efficient search techniques to find them.

**Signal injection:** In order to test the effectiveness of our search methods, we explore the topic of *signal injection*. We generate random Gaussian statistically isotropic full-sky maps based on our current $\Lambda$CDM best-fit cosmological model. Then, we artificially induce a signal in the map - for instance, by adding a cold spot of particular shape or size into the map. Finally, we use our existing techniques to search for the signal we added, to determine the efficiency of our search techniques and the minimum strength required for the signal before detection is possible. In this paper, we examine two specific signals: Hot and cold spots, and also multipole modulation, in which a particular direction of the sky is singled out.

**Results and conclusion:** Our results are somewhat disappointing; the techniques we studied require the signals to be quite large before detection at $3\sigma$ is possible. However, it is still useful to examine the topic; negative results are still worthy of being written up. At the least, this work will help us determine more efficient search techniques in the future, and provide a guideline on the sensitivity of our tools to detection of specific signals.

---

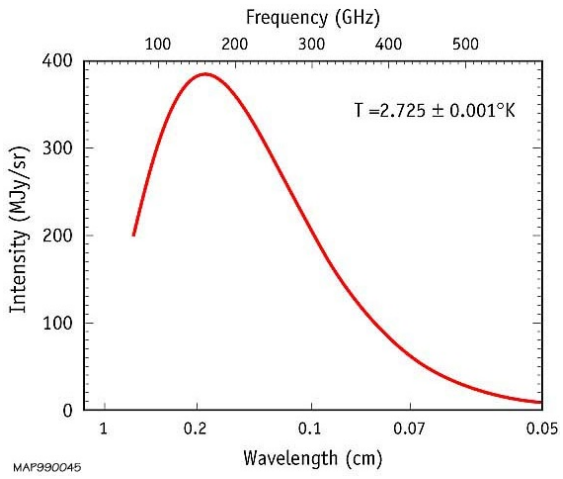[*] sophz@umich.edu
[†] huterer@umich.edu

FIG. 1: Graph of the cosmic microwave background radiation spectrum, measured by the FIRAS experiment on the COBE satellite. The curve is the theoretical prediction; all the data points lie within the thickness of the line, and cannot be visually distinguished from it. Indeed, the error bars are also thinner than the line, a fact indicating the stunning accuracy of the measurement, a strong confirmation of the Big Bang theory. Image credited to the COBE satellite team and NASA.

## I. INTRODUCTION AND BACKGROUND

The cosmic microwave background (CMB) consists of thermal black-body photons permeating the observable universe almost uniformly. Discovered serendipitously by Penzias and Wilson in 1964 [1], it was a strong confirmation for the Big Bang model of our universe.

The early universe was made up of a hot interacting plasma of photons, leptons, and baryons; as the universe expanded, the photons redshifted in wavelength, cooling until components of the universe decoupled one by one. Neutrinos, for instance, decoupled about 1 second after the Big Bang. When the universe was roughly $380,000$ years old, photons cooled to the point at which they could no longer ionize hydrogen, and thus formation of neutral hydrogen began, a process known as *recombination.* Before, photons could not freely travel, as they would continually scatter off free electrons and protons, but shortly after recombination, photons were able to travel freely ('free streaming') without interacting with matter; we view them as CMB photons today. They offer an unparalleled snapshot of the early universe, when it was less than a thousandth of its current age.

The cosmic microwave background is an almost perfect black-body spectrum. In Fig 1 above, we may see the CMB spectrum measured by the Far-Infrared Absolute Spectrophotometer (FIRAS) instrument on the Cosmic Background Explorer (COBE) satellite. It is the most precisely measured black body spectrum in nature, measured so accurately that the error bars and data points are thinner than the line (indicating the theoretical prediction.) The current temperature of the CMB is $T = 2.725 \pm 0.001$, where the error is not statistical, but rather refers to the scale of anisotropies in the cosmic microwave background. At this early stage, the universe was almost perfectly uniform, but those anisotropies grew over the course of its life to give us the clusters, galaxies, and overall structure we can see today. The CMB is believed to be statistically isotropic, though this is still a study of investigation today. Note the distinction between pure isotropy, in which everything is exactly the same in all directions, and statistical isotropy, in which the small anisotropies are Gaussian random without any innate pattern or preferred direction.

In addition to the anisotropies described above, the cosmic microwave background also has a dipole anisotropy, shown in Fig 2. This is caused by a Doppler shift in wavelength, due to the motion of the solar system through the rest frame of the CMB background. The dipole anisotropy is of order $10^{-2}$, a thousand times stronger than the fine structure of the CMB; it must be subtracted out carefully to see the detailed anisotropies. As a result of this velocity-induced dipole, it is impossible for us to measure the (much smaller) intrinsic dipole which should be present within the radiation. It was only after the launch of the Wilkinson Microwave Anisotropy Probe (WMAP) in 2003 that the CMB has could be measured in extremely detailed high-resolution full-sky maps [2–5]; these maps have been the subject of considerable study and examination over the past few years[6–9]. They will also be the main focus of this paper.

### A. Map methodology

We use WMAP's seven-year maps in our work [5]. Firstly, we use the ILC map, which attempts to reconstruct portions of the sky obscured by galactic noise; it is shown on the left panel of Fig 3. This is a risky process, however,
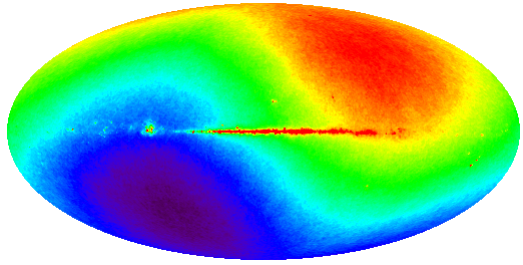
FIG. 2: This false color map is a Mollweide projection of temperatures in the cosmic microwave background; the dipole anisotropy visible is caused by a Doppler shift due to our motion relative to the cosmic microwave background. Note that the line around the equator of the map is caused by noise from the galaxy. Image credited to the WMAP satellite team and NASA.



$-400$ ▬▬ $400\,\mu K$

(a) Full-sky ILC map
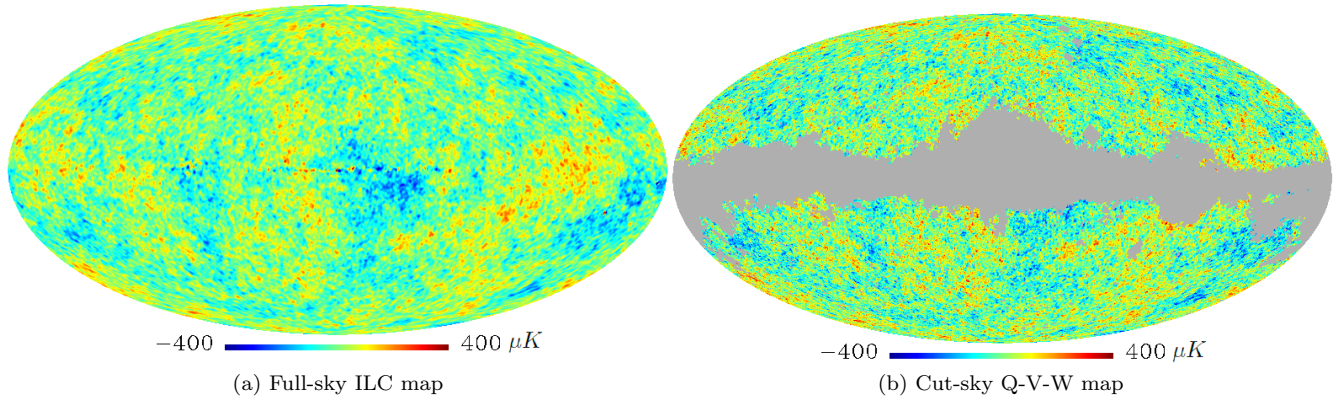


$-400$ ▬▬ $400\,\mu K$

(b) Cut-sky Q-V-W map

FIG. 3: The two figures are full-sky Mollweide projections of the cosmic microwave background (CMB), using 7-year data from the WMAP satellite. Note that the figures are in false color, with redder colors corresponding to warmer temperatures (and shorter wavelengths of photons), while bluer colors correspond to cooler temperatures. The figure on the left is the Internal Linear Combination (ILC) map, which attempts to subtract out the galactic foreground, reconstructing portions of the sky that would usually be obscured by noise. This is a risky procedure, however, which necessitates the assumption of statistical isotropy, and is only believed to be accurate on angular scales greater than 10°, according to the WMAP team. The right-hand figure is the coadded masked foreground-cleaned Q-V-W map; gray pixels represent points in the sky obscured by noise from the galaxy, or other point sources. Note that the ILC map has been smoothed through convolution with a Gaussian beam, removing much of the structure on smallest scales.

which includes the assumption of statistical isotropy. Although statistical isotropy is indeed a feature of our standard cosmological model, this assumption precludes our use of the map to test for statistical isotropy in the sky. In addition, the uncertainty involved within the procedure means that it is only accurate on large scales of $\gtrsim 10°$, according to the WMAP team.

In addition to the ILC map, we also use a map which has portions of the foreground remaining, but has not undergone risky reconstruction techniques. Specifically, we use a coadded masked foreground-cleaned Q-V-W map.

$$T = \frac{\sum_{r=3}^{10} T_r(i) w_r(i)}{\sum_{r=3}^{10} w_r(i)}, \tag{I.1}$$

where $T$ is the coadded temperature, determined from the weighted sum of temperatures $T_r$ of each individual radiometer $r \in \{Q1, Q2, V1, V2, W1, W2, W3, W4\}$, divided by the total weight. The weights at each pixel for each radiometer are $w_r(i) = N_r(i)/\sigma_r^2$, where $N_r(i)$ are the number of effective observations at the pixel, and $\sigma_r$ is the noise dispersion for the given receiver

This coadding was performed on maps at resolution of $N_{\text{side}} = 512$ ($\sim 8'$). Finally, we applied the KQ75 mask, a pixel mask provided by the WMAP team to exclude foreground-contaminated regions of the sky from analysis. The resultant map may be seen in the right panel of Fig 3.
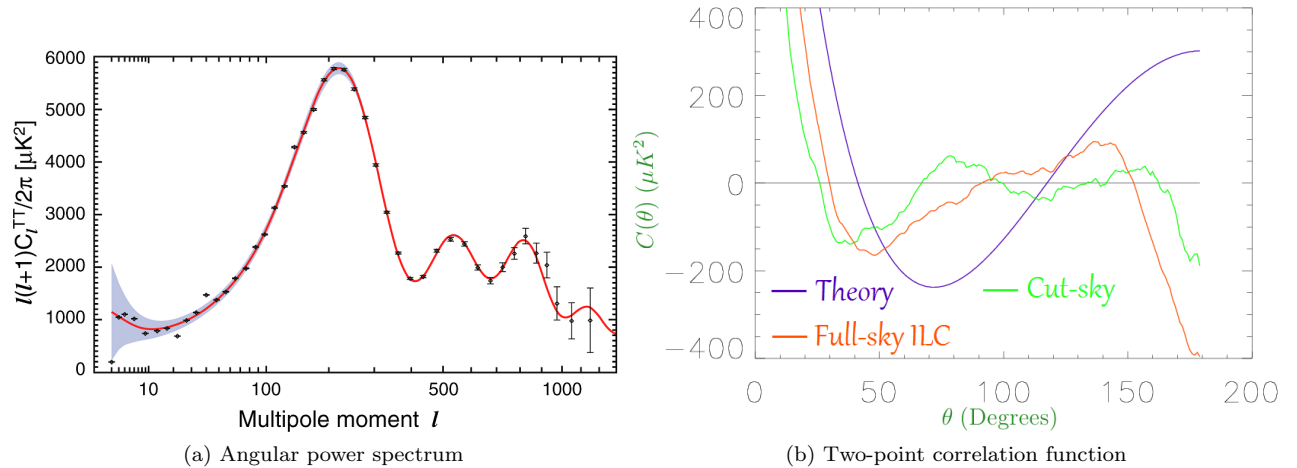
(a) Angular power spectrum                                    (b) Two-point correlation function

FIG. 4: *Left:* Power spectrum of the CMB. Points are WMAP measurements, while the red line is the best-fit curve in our $\Lambda-$CDM model. The gray bands signify cosmic variance - the model results are the expected average over an ensemble of universes, but we have only one universe to observe. The first point is the quadrupole, which is seen just below the error band and considerably less than the expected value. Image credited to the WMAP satellite team and NASA. *Right:* The angular correlation function in the CMB $C(\theta) = \overline{T(\hat{\Omega}_1), T(\hat{\Omega}_2)}\Big|_{\hat{\Omega}_1 \cdot \hat{\Omega}_2 = \cos\theta}$. The $\Lambda-$CDM theoretical prediction is in purple, while the result from the ILC map is depicted in red, and the result from the foreground-cleaned coadded Q-V-W bands map is delineated in green. The green curve is unusually close to 0 past $\theta \approx 60°$. Data is from WMAP

## II.   CLAIMED ANOMALIES IN THE CMB

There have been a number of claimed anomalies in the cosmic microwave background. In this section, we will briefly cover the most prominent ones, to give an idea of the signals we would like to detect.

### A.   Cold Spot

Since the WMAP 3rd-year data release, work has been done suggesting the presence of an anomalously cold spot in WMAP data centered in the southern hemisphere, at galactic coordinates $(l, b) = (208, -56)$ [10–12]. The spot is of size roughly $4.6°$ in radius, and has an *a priori* significance of $\approx 10^{-3}$ (0.1%). Suggestions have been made that the spot is due to a void or cosmic texture, among other explanations.

In 2009, a paper by Zhang and Huterer [13] called the significance of the spot into question. Namely, it claimed that the quoted statistics were a priori and the actual significances were not unusual enough for a discovery.

### B.   Low quadrupole problem

Since the analysis of data from the Cosmic Background Explorer (COBE) satellite, the quadrupole ($l = 2$) moment of the CMB is known to be considerably lower than expected; this is shown in the left panel of Figure 4. However, due to cosmic variance (the model prediction is for an average over an entire ensemble of universes, whereas have only one universe to observe) and foreground contamination through dust and synchrotron/free-free emission, errors are considerably high. A full Bayesian analysis by O'Dwyer *et al.* [14] has shown that the quadrupole is significant only at the 10% level.
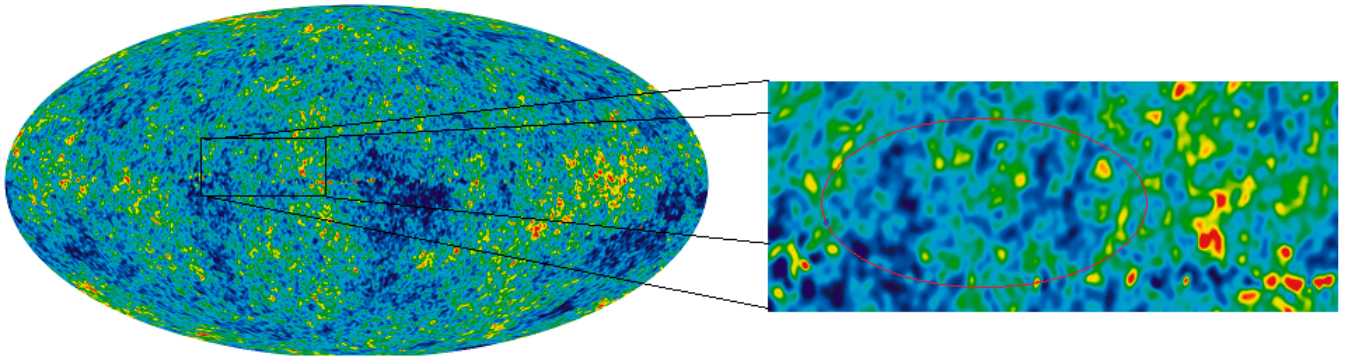
4

FIG. 5: It transpires that using the Internal Linear Combination (ILC) map with the right temperature scales, it is possible to see temperature fluctuations that look like the initials "S H" - perhaps short for Stephen Hawking. This demonstration of *a priori* statistics and cosmic coincidences was originally noted by Lyman Page, and later used as an example by Bennett *et al.* [23].

### C.    Lack of angular correlations

The angular correlation function $C(\theta)$ is defined as the average product in temperature between two points separated by degree $\theta$. That is,

$$C(\theta) = \overline{T(\hat{\Omega}_1), T(\hat{\Omega}_2)}\Big|_{\hat{\Omega}_1 \cdot \hat{\Omega}_2 = \cos \theta} \tag{II.1}$$

$C(\theta)$ and the power spectrum $C_l$ are related through the relation

$$C(\theta) = \sum_{l=2}^{\infty} \frac{2l + 1}{4\pi} C_l P_l(\cos \theta) \tag{II.2}$$

Measurement of $C(\theta)$ in our sky has shown it to diverge considerably from $\Lambda-$CDM model predictions, as shown in the right panel of Fig 4. Moreover, it is observed that in the cut-sky, $C(\theta)$ is unusually close to 0 for $\theta \geq 60°$. [1]

In order to quantify the low power in the angular two-point function between approximately $60°$ and $180°$, the statistic [15]

$$S_{1/2} = \int_{-1}^{1/2} C(\theta)^2 d(\cos \theta) \tag{II.3}$$

has been widely used. Analysis has shown the result in our sky to be significant at a level of $\geq 3.2\sigma$ [16–18], though the validity of this result has been questioned [19]. A recent analysis by Zhang [20] suggests that the result may be related to the regions of the sky corresponding to the quadrupole and octupole.

### D.    Alignment of quadrupole and octupole vectors

While the power spectrum plots the magnitude of the multipoles, each of them also have directional vectors associated with them (See Section IV B for more details). Analysis has shown [6, 21, 22] that the quadrupole and octupole vectors are strangely aligned with each other and the ecliptic plane, jokingly dubbed by researchers as the "axis of evil." This alignment is especially strange as the ecliptic plane is simply the plane of Earth's orbit around the Sun, devoid of cosmological significance.

--------

[1] Here, I am discussing the results in the cut-sky map; as mentioned earlier, the full-sky ILC map is known to be unreliable for detailed analysis.

### E.   WMAP team response Response

The WMAP team examined the claimed anomalies and concluded that no significant anomalies existed [23]. They stated that the claims were mostly the product of a-posteriori statistics. To illustrate their point, WMAP pointed out that using the ILC map, with the temperature scales set right, it is possible to see Stephen Hawking's initials in the CMB. This is illustrated in Figure 5

Of course, there are many caveats to this example - the image only shows up in the ILC map, in which galactic noise is subtracted out through assuming statistical isotropy, the temperature scale has to be set in a certain manner, etc. Nevertheless, it is a useful example that patterns do not have to have a meaning; the human eye in particular has a tendency to see 'patterns' within random data (phenomenon known as apophenia and pareidolia.) In order to have robust results, we must be careful to avoid *a priori* statistics.

## III.   HOT AND COLD SPOTS

In order to test for anomalies in the cosmic microwave background, we must first devise efficient search techniques capable of detecting potential anomalies. As a result, we have an interest in testing the sensitivity of our methods and their facility for signal detection. We now seek to artificially inject 'signals' into arbitrary skies and detect the artificial results through our array of search techniques.

One of the simplest types of CMB anomalies are the potential existence of unusually 'hot' or 'cold' spots; study in this area has focused around the claimed WMAP cold spot, following the work of [10]. In this section, we examine injection of simple hot or cold spots of varying shape, size, and radius into the cosmic microwave background. We then attempt to search for the artificial signals using different weight functions in our search, and compare them to results for unmodified random skies.

### A.   Weight function methodology

We consider three different weight functions: Top-hat weights (disks), Gaussians, and Spherical Mexican Hat Wavelets. This analysis is based around the previous work of Zhang and Huterer [13]

We define the disk top-hat weight of radius $R$ as

$$D(r) \equiv A_{\text{disk}}(R) \left[\Theta(r) - \Theta(r - R)\right], \tag{III.1}$$

where $\Theta(r)$ is a Heaviside step function and $A_{\text{disk}}(R) = (2\pi(1 - \cos(R)))^{-1/2}$ is defined so that

$$\int_0^\pi D(r)^2 d\Omega = 1. \tag{III.2}$$

Note however that the normalization $A_{\text{disk}}(R)$ is unimportant for our analysis, as we perform relative comparisons of temperatures in disks on the sky. The top hat-weighted temperature coefficients are given by

$$T_{\text{disk}}(\hat{r}; R) = \int d\Omega' T(\hat{r}') D(\alpha; R), \tag{III.3}$$

where $\hat{r} = (\theta, \phi)$ is the location of a given spot, $\hat{r}' = (\theta', \phi')$ is the dummy location on the sky whose temperature we integrate over, and $\alpha = \arccos(\hat{r} \cdot \hat{r}')$ is the angle between the two directions.

Our Gaussian weights are defined similarly. The weight functions are

$$G(r) \equiv A_{\text{Gauss}}(R) \exp\left(-4\ln 2 \frac{r^2}{R^2}\right), \tag{III.4}$$

so that the full width at half maximum of the distribution is equal to $R$. The weighted temperatures are given by

$$T_{\text{Gauss}}(\hat{r}; R) = \int d\Omega' T(\hat{r}') G(\alpha; R). \tag{III.5}$$

Finally, we use wavelet search functions, with procedure following the work of Cayon *et al.* [24], Martinez-Gonzalez *et al.* [25]. The Spherical Mexican Hat wavelets are defined as

$$\Psi(\theta; R) = A_{\text{wav}}(R) \left(1 + \left(\frac{y}{2}\right)^2\right)^2 \left(2 - \left(\frac{y}{R}\right)^2\right) \exp\left(\frac{-y^2}{2R^2}\right), \tag{III.6}$$

where $y \equiv 2\tan(\theta/2)$ and

$$A_{\text{wav}}(R) = \left[2\pi R^2 \left(1 + \frac{R^2}{2} + \frac{R^4}{4}\right)\right]^{-1/2}, \tag{III.7}$$

so that $\int d\Omega\, \Psi^2(\theta; R) = 1$ over the whole sky. We may now define the continuous wavelet transform stereographically projected over the sphere with respect to $\Psi(\theta; R)$, with $T$ being the CMB temperature:

$$T_{\text{wav}}(\vec{x}; R) = \int d\Omega' T(\vec{x} + \vec{\mu}')\Psi(\theta'; R), \tag{III.8}$$

where $\vec{x} \to (\theta, \phi)$ and $\vec{\mu}' \to (\theta', \phi')$ are the stereographic projections to the sphere of the center of the spot and the dummy location, respectively, and are given by

$$\vec{x} = 2\tan\frac{\theta}{2}(\cos\phi, \sin\phi), \tag{III.9}$$

$$\vec{\mu}' = 2\tan\frac{\theta'}{2}(\cos\phi', \sin\phi'); \tag{III.10}$$

see Martinez-Gonzalez *et al.* [25] for details. To work in terms of purely spherical coordinates, we center the spot location to the north pole of the sphere, and rewrite the above as

$$T_{\text{wav}}(\hat{r}; R) = \int d\Omega' T(\hat{r}')\Psi(\alpha; R), \tag{III.11}$$

where $M(\hat{r}')$ is the mask, defined to be 1 for pixels within the mask and and 0 for those outside of it. For ease of computation, we cut off the integral at values of $\alpha = 4R$, as the wavelet is effectively zero for greater values. Afterwards, we may carry out the integral by using the Healpix command `query_disc` to find all pixels within that radius from the wavelet center.

## B.   Significance statistics

To find the coldest spots in each sky, we evaluate the weighted temperatures

$$T_{\text{Weight}}(\hat{r}; R) = \int d\Omega' T(\hat{r}')W(\alpha; R) \tag{III.12}$$

where $W(\alpha; R)$ is the weight function (either top-hats, Gaussians, or wavelets), and $\hat{r} = (\theta, \phi)$ is the location of a specific spot.

The locations of centroids of spots are chosen to be all the centers of pixels in $N_{\text{side}} = 32$ resolution; therefore, we examine $N_{\text{pix}} = 12\, N_{\text{side}}^2 \sim 12,000$ spots on the sky. In order to calculate the spots' weighted temperatures, however, we analyze the coadded map at resolution of $N_{\text{side}} = 128$ ($\sim 0.5°$), which is sufficiently high to allow our results to converge for spots of $R \gtrsim 2°$ , but still low enough to be numerically feasible.

For our statistic, we use the temperature of the coldest spot divided by the standard deviation of the distribution of all spots

$$S_{\text{Weight}}(R) \equiv \frac{T_{\text{disk}}^{\text{coldest}}(R)}{\sigma_{\text{disk}}(R)} \tag{III.13}$$

and equivalently for the Gaussian weights and the wavelets. Here $\sigma_{\text{disk}}(R)$ is the standard deviation of the distribution of all spots in a given map, while $T_{\text{weight}}^{\text{coldest}}(R)$ is the coldest spot for a given weight and given scale in the distribution.

(a) Wavelet calculations on the full-sky ILC map



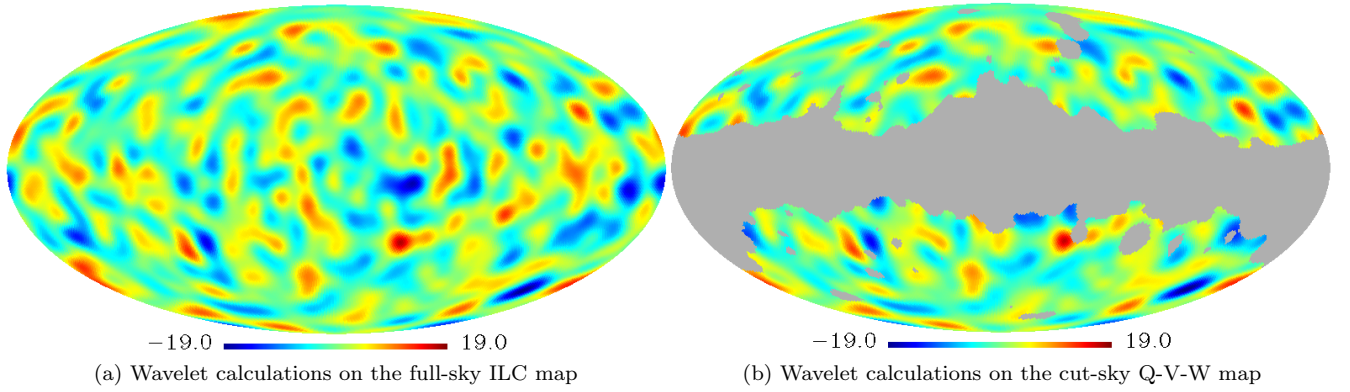(b) Wavelet calculations on the cut-sky Q-V-W map

FIG. 6: Depicted above is a demonstration of our methodology for finding coldest spots in each map. These two figures are not conventional temperature maps, but Mollweide projections of the temperatures *weighted by 5-degree Spherical Mexican Hat Wavelets*. That is, for each pixel $\hat{\Omega}$ plotted above, the value of that pixel in the map is $M(\hat{\Omega}) \equiv T_{\text{wav}}(\vec{x}; R = 5) = \int d\Omega' T(\vec{x} + \vec{\mu}')\Psi(\theta'; R = 5)$. The left plot shows values evaluated for the full-sky ILC map; the right plot shows values evaluated for the coadded masked foreground-cleaned Q-V-W map; calculations were performed at $N_{\text{side}} = 128$. After calculating the above, we may then determine $T_{\text{wavelet}}^{\text{coldest}}(R = 5)$ for these specific maps (and repeat the process for each new map, radius size, and weight function.) Note that the large dark blue (cold) region in the lower right of both figures is the 'cold spot', claimed to be anomalous by Cruz *et al.* [10]

Note that the distribution of spot temperatures is not Gaussian, as the spots overlap and are not independent. We scale $T$ by $\sigma$ in Eq. (III.13) in order to account for small ($\sim 10\%$) differences in the overall level of power in spots of characteristic size $R$ in the different maps — in effect, $\sigma_{\text{disk}}(R)$ provides units in which to best report the coldest temperature. In unaltered random maps, we use a range of $R \in \{2°, 2.5°, \ldots, 9°\}$ for disk and Gaussian weights, and a reduced range of $R \in \{2°, 2.5°, \ldots 6.5°\}$ for wavelet weights. [2]

Computing the significance of our statistic $S_{\text{disk}}(\hat{r}; R)$ is then in principle straightforward: we compare it to values obtained from simulated Gaussian random maps and rank-order it; the rank gives the probability.

Finally, to avoid *a priori* statistics when comparing statistics to random maps, we also form an overall statistic, which is defined as the minimum value of our statistic $S_{\text{Weight}}(R)$ (defined in Eq III.13) over a range of scales $R$.

$$S_{\text{overall}}(\text{Weight}) \equiv \min_{R}\{S_{\text{Weight}}(R)\} \tag{III.14}$$

where

$$R \in \{2°, 2.5°, \ldots, 9°\} \tag{III.15}$$

$$\text{Weight} \in \{\text{wavelet}, \text{disk}, \text{Gaussian}\}$$

as well as a 'superstatistic', adopted from Zhang and Huterer [13], which is defined as the minimum *a priori* probability across the same range of scales

$$S_{\text{super}}(\text{Weight}) \equiv \min_{R}\{P(\text{Weight, R})\} \tag{III.16}$$

over the same range of scales as above, where the specific *a priori* probabilities are calculated by comparison to other Gaussian random maps. So for instance, if a map is ranked #4 in coldness for Gaussian spots of radius 5° out of the 10,000 random maps, then that map has $P(\text{Weight=G, R} = 5°) = \frac{4}{10,000} = 0.04\%$

————

[2] For wavelets with $6.5° \leq R \leq 9°$ the calculations at $N_{\text{side}} = 128$ were unfeasible due to the large number of pixels to keep track of. As a result, we only consider scales of $2° \leq R \leq 6.5°$ for wavelet weight functions, but consider the full range $2° \leq R \leq 9°$ for disks and Gaussians.
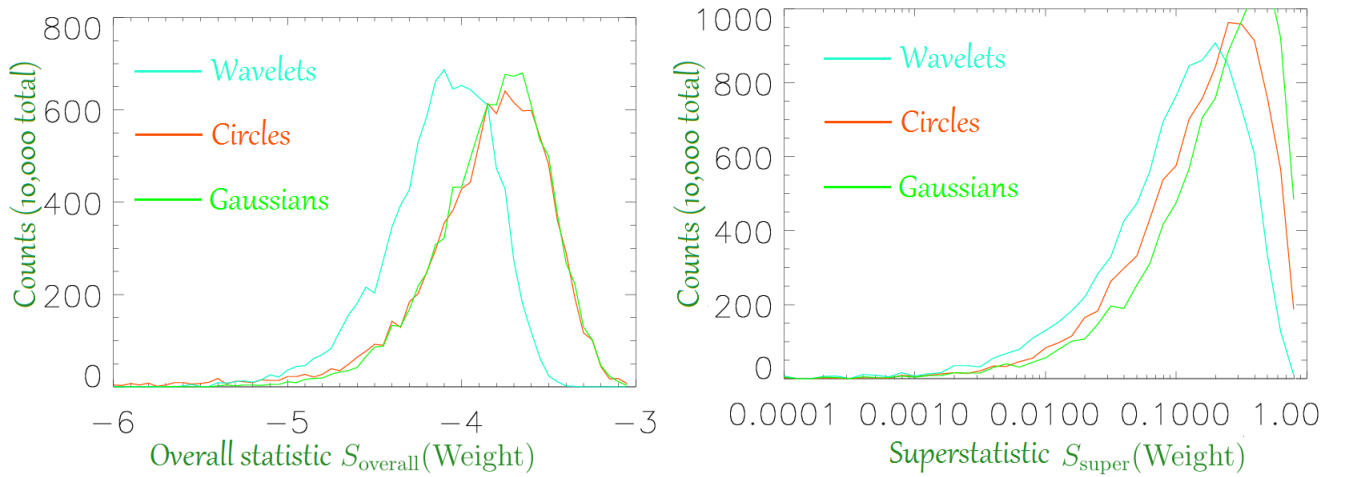
FIG. 7: We plot a histogram for the range of overall statistics $S_{\mathrm{overall}}(\mathrm{Weight})$ and superstatistics $S_{\mathrm{super}}(\mathrm{Weight})$ (logarithmic scale) for each of the 10,000 specific random Gaussian maps. We find that wavelets appear to be a more 'efficient' weight function for searching for signals. That is, looking at Gaussian random maps across a range of radii, you are more likely to find an 'anomalous' *a priori* $3\sigma$ result with wavelets than with circles and gaussians.
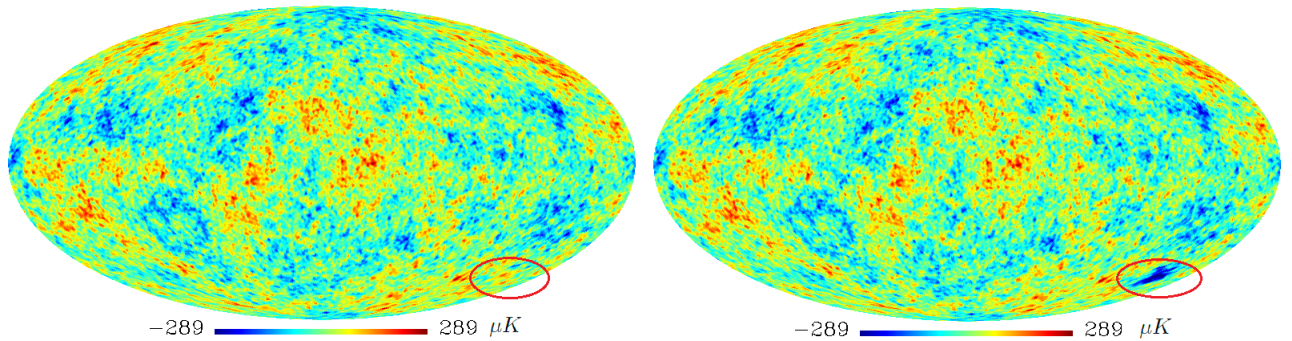


FIG. 8: An example of a random Gaussian map before (left) and after (right) a Gaussian-shaped signal of radius $8°$ is artificially added; the region in question is circled in red.

### C.   Random map statistics

For our analysis, we used 10,000 randomly generated Gaussian full sky maps. The skies have been generated using the Healpix facility `synfast`, and used as input the power spectrum determined in the WMAP 7-year analysis. The maps were then smoothed by a Gaussian with FWHM $= 1°$ to match the WMAP procedure.

Our findings are shown in Fig 7. We find that wavelets are inherently superior at finding signals; looking at Gaussian random maps across a range of radii, you are more likely to find an 'anomalous' *a priori* $3\sigma$ result with wavelets (1.62% likely) than with circles (0.76% likely) and gaussians. This is because wavelets are able to filter out correlation between different scales.

As we calculate probability by comparison to other Gaussian random maps, the total number of $3\sigma$ results across the spectrum of random maps and radii is constant [3], at

$$N_{3\sigma} \equiv 0.27\% \times N_{\mathrm{Maps}} \times N_{\mathrm{Radii}}. \tag{III.17}$$

———

[3]Note that due to computational complexity issues, we only computed $2 < R < 6.5°$ for wavelets, as opposed to $2 < R < 9°$ for circles and Gaussians, and hence would have reason to expect fewer maps with $3\sigma$ results for wavelets, simply due to a smaller search range.
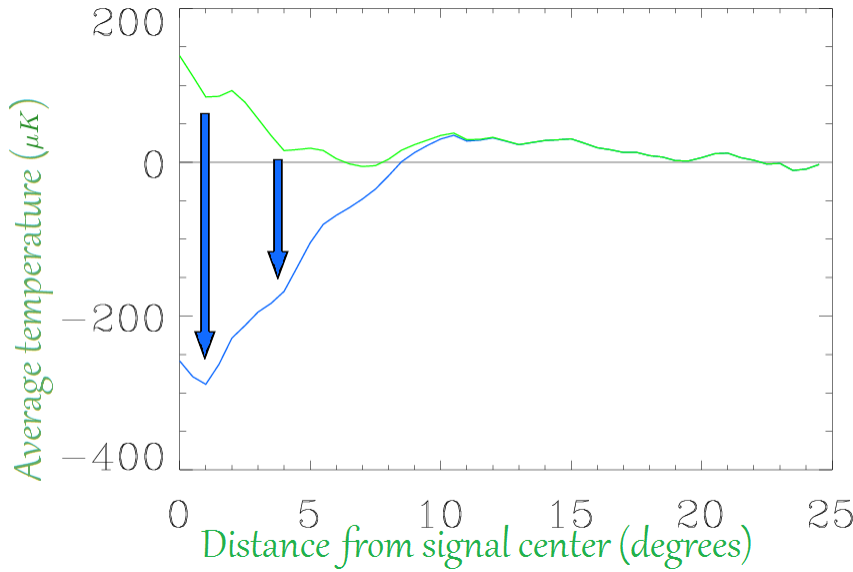
FIG. 9: We plot the average temperature distribution of points with respect to their distance from the center of the signal. In green is the temperature distribution for the pre-signal random map; in blue, we see the temperature distribution for the map after a Gaussian-shaped signal with radius of $8°$ has been injected into the map. Note that the (randomly chosen) signal center was, by chance, a 'hot spot' with positive temperature; as a result, the signal has lost part of its strength working against the intrinsic temperature anisotropy of the map.
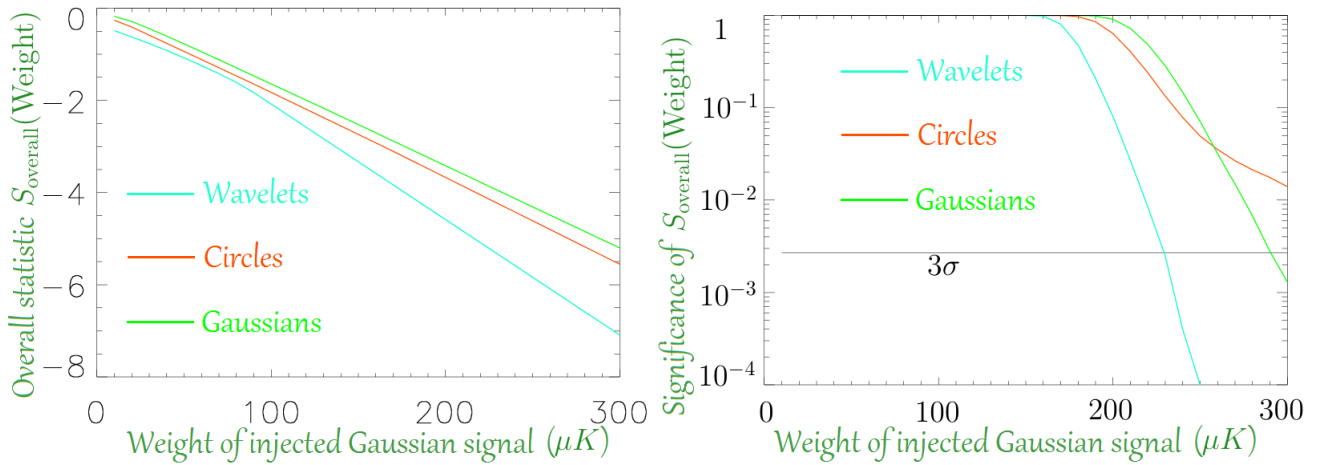


FIG. 10: Our attempts at detecting the significance of a sample signal. The left graph plots $S_{\mathrm{overall}}(\mathrm{Weight})$ with respect to the signal strength. The right graph plots the *significance* with respect to random maps of $S_{\mathrm{overall}}(\mathrm{Weight})$; the black line denotes a probability of $3\sigma$ (0.27%). It appears that wavelets are superior at detecting signals. In addition, the signal needs to be quite strong ( $\approx 250\mu K$) before it can be detected at a true significance of $3\sigma$ (having accounted for *a priori* statistics.)

The difference comes because wavelets more efficiently distribute their result across multiple maps. For instance, if a specific random map has a $3\sigma$ result with $R = 5°$ circles (or Gaussians), it is likely to also have a low-probability result for $R = 4°, 4.5°$,etc. circles (or Gaussians); thus, the spectrum of $3\sigma$ results is tightly clustered across specific maps for circles or Gaussians. Wavelets suffer less from this issue, and hence, it is more likely to find an *a priori* $3\sigma$ result with wavelets than with other weight functions. To avoid *a priori* statistics, we must take this effect into account when examining signal injection into random skies; otherwise, wavelets will appear to be more effective than they actually are.

### D.   Signal injection and results

We now experiment with injecting cold spot signals of arbitrary size into Gaussian random statistically isotropic skies generated from the underlying best-fit $\Lambda-$CDM cosmological model. For simplicity, we select the shapes of the signals to be our three weight functions - top hats, Gaussians, and wavelets. Plotted in Fig 8 is an example of a random sky before and after the signal is injected; Fig 9 shows how the radial temperature distribution (centered

around our signal) changes before and after we artificially add the signal to the sky. Note that by happenstance, our signal was injected on top of an intrinsic 'hot spot' temperature anisotropy. This highlights that there is an element of uncertainty to signal injection - if, by chance, our artificial cold spot is added on top of an intrinsic hot spot of similar size and magnitude, the two could cancel out, leaving little trace. On the other hand, if - by random chance - we begin with a Gaussian sky which improbably already contains an extraordinarily cold spot, then no signal would be needed for us to detect an apparently anomalous result.

After adding the artificial signal into a section of the sky, we then attempt to detect it with the weight functions described above.

Our findings appear to be qualitatively consistent across a range of signal shapes and radii. An example is shown in Fig 10, for an $8°$ Gaussian signal. We find that unfortunately, the signal needs to be quite strong (150-200 $\mu$K) before we may obtain an *a priori* significance of $3\sigma$. Furthermore, it appears that the wavelet is somewhat superior at detecting signals regardless of their shape, even after accounting for *a priori* statistics.

## IV.   MULTIPOLE VECTORS

We now move on from our study of hot and cold spots, and consider the use of multipole vectors to search for anomalies.

### A.   Anisotropy decomposition

One commonly used method of studying the CMB, is to decompose anisotropies in the sky into spherical harmonics

$$T(\hat{\Omega}) - \overline{T(\hat{\Omega})} = \sum_{l=1}^{\infty} \sum_{m=-l}^{l} a_{lm} Y_{lm}(\hat{\Omega}) \tag{IV.1}$$

$$C_l = \frac{1}{2l+1} \sum_{m=-l}^{l} |a_{lm}|^4 \tag{IV.2}$$

In the first equation, we take the temperature difference as a function of vector $\hat{\Omega}$ in the sky, and express it with a spherical harmonic summation. In the second equation, we condense the power of each angular scale $l$ into a single measure $C_l$, the power spectrum, which agrees well with predictions through the standard $\Lambda CDM$ cosmological model.

However, the measure above loses directional information which may be present in correlations between the individual $a_{lm}$s. As the assumption of statistical anisotropy has been questioned due to the discovery of various claimed anomalies in the CMB [10, 23], it may be useful to create a new measure which retains directional information. This was done by Copi, Huterer, and Starkman [26], by proposing the method of multipole vector decomposition to express anisotropies in the CMB sky [17, 27].

### B.   Vector decomposition

The idea of multipole vector decomposition is to construct a set of $l$ unit vectors $\hat{v}^{(l,i)}|_{0 \leq i \leq l}$ and a scalar $A^{(l)}$ from each multipole moment, $\sum_{m=-l}^{l} a_{lm} Y_{lm}(\hat{\Omega})$. That is, we express

$$\sum_{m=-l}^{l} a_{lm} Y_{lm}(\hat{\Omega}) \approx A^{(l)} (\hat{v}^{(l,1)} \cdot \hat{e})...(\hat{v}^{(l,l)} \cdot \hat{e}) \tag{IV.3}$$

$$\sum_{m=-l}^{l} a_{lm} Y_{lm}(\hat{\Omega}) \approx A^{(l)} \Pi_{i=1}^{l} (\hat{v}^{(l,i)} \cdot \hat{e}) \tag{IV.4}$$

$l=1$                                  $l=2$

$-250$ ▬▬▬ $250\ \mu K$        $-250$ ▬▬▬ $250\ \mu K$

$l=3$                                  $l=4$

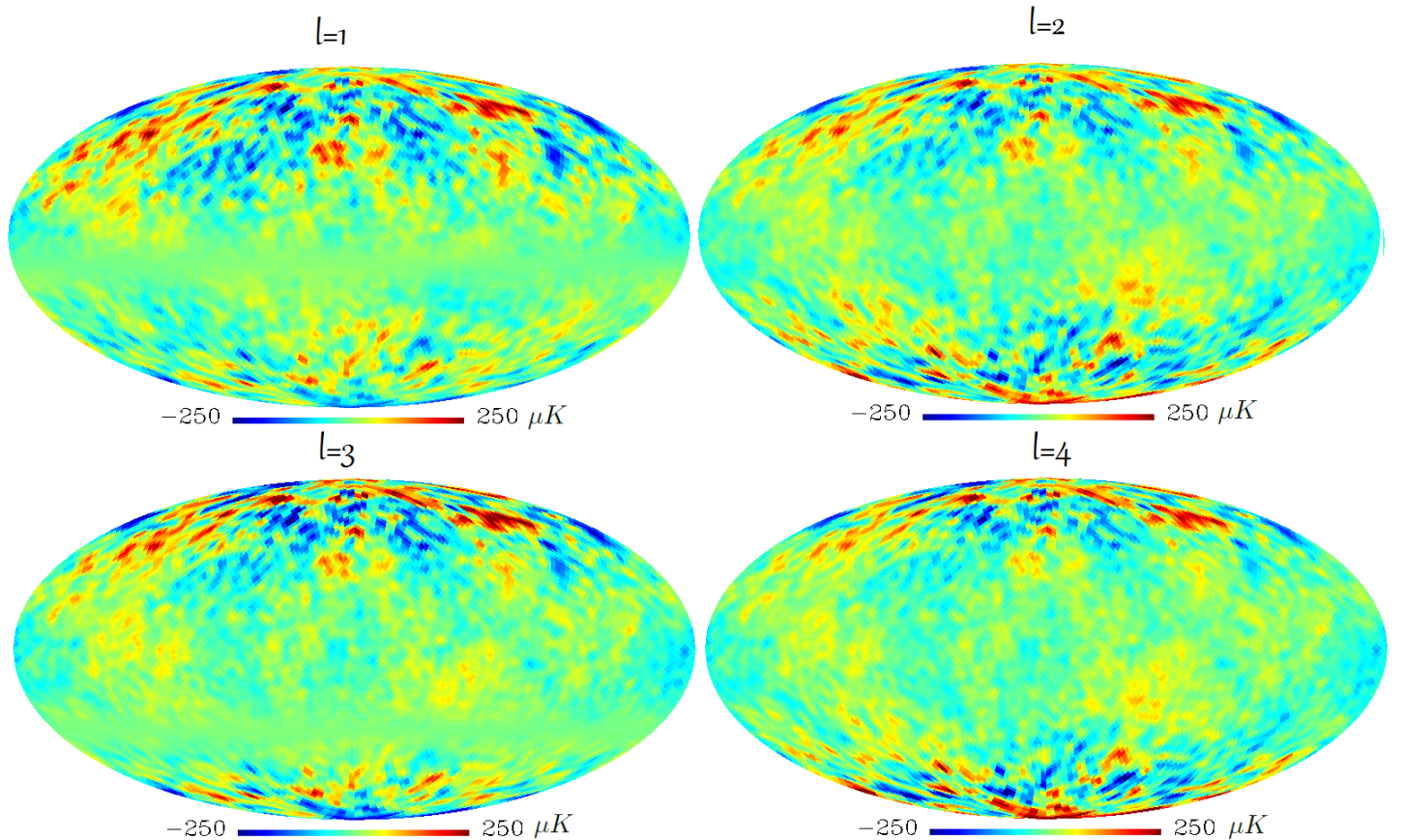$-250$ ▬▬▬ $250\ \mu K$        $-250$ ▬▬▬ $250\ \mu K$

FIG. 11:

Mollweide projections of skies which have undergone multipole modulation $T_{\text{new}}(\hat{\Omega}) = T_{\text{old}}(\hat{\Omega})[1 + A(\hat{\Omega} \cdot \hat{n})^l]]$ in the +z direction in galactic coordinates, with A=5 (a very strong modulation. By comparison, the best-fit value for our fiducial sky is $A \approx 0.072$ [7]. In the upper left is a dipole ($l = 1$) modulated sky; upper right is a quadrupole ($l = 2$) modulated sky; lower left is a octupole ($l = 3$) modulated sky; lower right is a hexadecapole ($l = 4$) modulated sky. The temperature scale is identical between all four sky plots.

For more details regarding the computation of multipole vectors, see [26]. We reuse the multipole vector decomposition code of Copi et al., which is publicly available from their website.[4]

### C.   Detection of injected dipole modulation signals

One widely considered possible background in the CMB is a dipole modulation [7, 28–30].

$$T_{\text{new}}(\hat{\Omega}) = T_{\text{old}}(\hat{\Omega})[1 + A(\hat{\Omega} \cdot \hat{n})] \tag{IV.5}$$

Here, $\hat{n}$ is the modulation direction and $A$ is the modulation strength. Note that this is different from the $l = 1$ multipole (dipole), as this multiplies the temperature anisotropies, whereas the dipole is additive. The net effect on the sky is more complicated than in the equation above, as injecting such a dipole modulation would also create a dipole, which is typically removed [5] We wish to investigate the possibility of detecting such a background signal through use of multipole vectors.

---

[4]http://www.phys.cwru.edu/projects/mpvectors

[5]The intrinsic CMB dipole cannot be seen, as it is drowned out by the much larger Doppler shift dipole caused by the peculiar velocity of our solar system through the cosmos; hence, it is standard practice to remove the dipole.
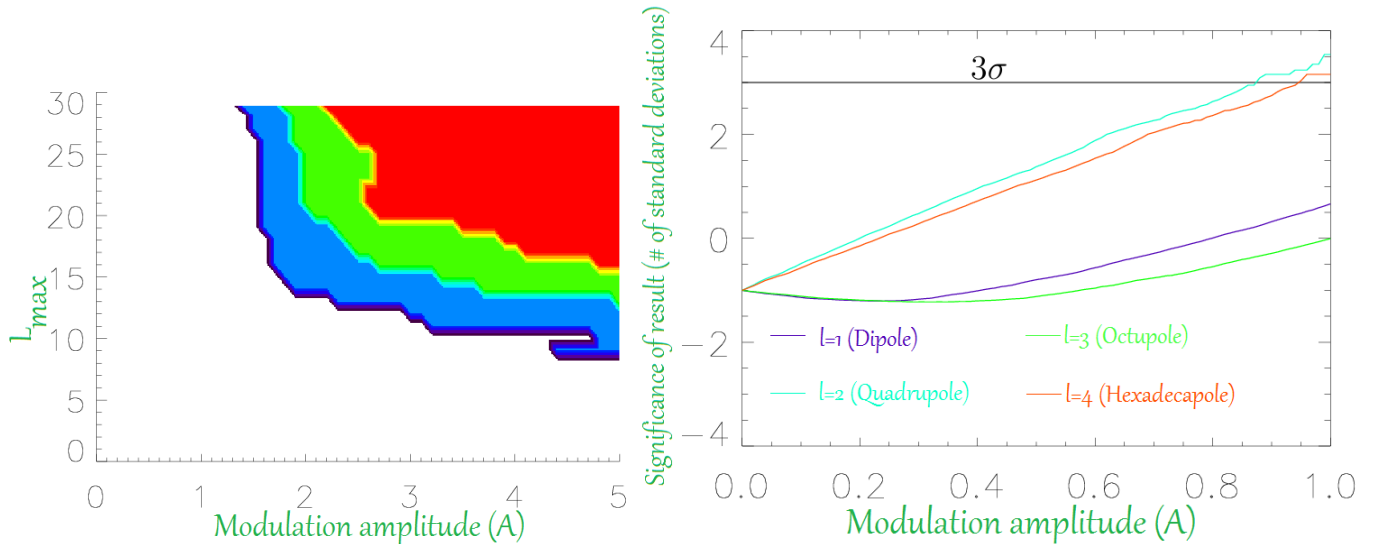
FIG. 12: *Left:* A contour plot with the x-axis being the strength of the modulation (A) and the y-axis being the maximum multipole $l$ considered in the statistic. The three contours are for $1\sigma$, $2\sigma$, and $3\sigma$. Thus, considering more multipoles (and more vectors) increases the statistics, meaning that a smaller modulation amplitude is needed to reach $3\sigma$ significance. *Right:* We plot the significance of results with respect to the modulation amplitude $A$, for modulation of orders $l = 1, 2, 3, 4$ (where we have assumed a Gaussian distribution.) Our signal is injected into a random maps with initial statistic $-1\sigma$ (Eq IV.7.) The four colored curves are the results for the dipole ($l = 1$, in purple), quadrupole ($l = 2$, in light blue), octupole ($l = 3$, in green), and hexadecapole ($l = 4$, in red.) The black line represents a $3\sigma$ result. The general trend continues for higher multipole values - our statistic is much better at detecting even-order modulation than odd-order modulation. In addition, its effectiveness declines as the order of modulation increases. Thus, it is most effective at detecting $l = 2$ quadrupole modulation

For this analysis, we use the statistic

$$S \equiv \sum_{l=2}^{L_{max}} \sum_{i=1}^{l} (\hat{v}^{(l,i)} \cdot \hat{n})^2, \tag{IV.6}$$

chosen for simplicity. We square before summing, because dipole modulation biases the multipole vectors not only towards the modulation direction, but also the opposite point on the sphere (in short, we wish $\hat{v}^{(l,i)} \cdot n = -1$ to be considered just as significant as $\hat{v}^{(l,i)} \cdot n = +1$.) Practically, due to computational constraints we will need to cut off the sum over $l$ at some point (which we designate $L_{max}$.)

For our analysis, we generate 5,000 Gaussian random statistically isotropic maps, based on the underlying best-fit $\Lambda$CDM cosmological model. For simplicity, we do not apply a mask (this is because a masked sky complicates the method for recovering the $a_{lm}$s).

We inject a modulation signal of varying strength ($A$) into a random sky and compare the value of our statistic (selecting $\hat{n}$ to be that of the injected dipole modulation) to that of the other randomly generated skies. We also vary the maximum $l$ over which we sum, to ascertain if a balance can be struck between statistics and computational complexity.

The results, shown in the left panel of Figure (12), are discouraging. Very high modulation amplitudes ($A \geq 1.5$, compared to fiducial $A \approx 0.072$) are required to reach $3\sigma$ significance, and the overall trend of the contour seems to indicate that increasing statistics by increasing the maximum $l$ in our summation will not improve matters by much.

It must also be noted that even this discouraging result is optimistic, as it neglects several issues. Firstly, the statistic we used measures the correlation of vectors to the modulation direction in unmodulated random maps - essentially, examining correlation to a random direction. To properly compute the statistics, one would find the best-fit modulation direction for every single unmodulated random map.
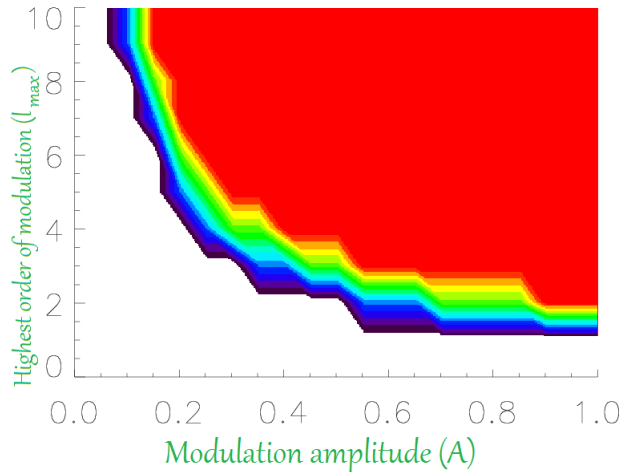
FIG. 13: Depicted here is a contour plot with the x-axis being the strength of the modulation (A) and the y-axis being the order of modulation $l$ (with $l = 1$ being the dipole modulation we previously considered, for instance.) The three contours are for $1\sigma$, $2\sigma$, and $3\sigma$.

In addition, the statistics also depend on the correlation of vectors in the starting map to which you wish to inject a dipole modulation. To illustrate with an example, imagine a hypothetical randomly generated map whose multipole vectors through sheer coincidence all align perfectly towards the same direction. Obviously, the statistic for this map would then be above $3\sigma$ even if no modulation would be added. For our results, we started with a random map whose correlation is $\approx 1\sigma$ below the mean compared to other random skies (i.e. for $A = 0$, the statistic is $-1\sigma$), so the $3\sigma$ bound we computed should be valid for $\approx 82\%$ of starting maps (if we neglect the first caveat above); computational time constraints did not permit the use of a wide range of initial random maps. The point, in short, is that the contours are not clearly delineated, as their exact location depends on the starting map.

### D.   Multipole modulation

One of the reasons behind our poor results with dipole modulation is that most of its effect is deposited within the l=1 dipole - which is removed and hence not considered within our statistic. To rectify this problem, we consider a different signal, a generalized multipole modulation.

$$T_{\text{new}}(\hat{\Omega}) = T_{\text{old}}(\hat{\Omega})[1 + A(\hat{\Omega} \cdot \hat{n})^l]] \tag{IV.7}$$

Here, $l$ is a constant denoting the order of our modulation. For instance, $l = 1$ gives the dipole modulation discussed earlier, but we may also have $l = 2$ (quadrupole modulation), $l = 3$ (octupole modulation), and so on for arbitrary l. Thus, keeping the statistic defined above, we seek to vary $l$ and the modulation amplitude $A$ to determine if it is possible to detect small signals for higher orders of modulation with the multipole statistic we have previously defined.

Our results, shown in the right panel of Figure 12, are interesting. It appears that the selected statistic is very good at detecting even-order modulations (e.g. l=2, l=4, etc.) but exceedingly poor at detecting odd-order modulations (e.g. l=1, l=3, l=5.) This serves as an explanation to our earlier lack of success in dipole modulation. Furthermore, the statistic becomes less effective when examining higher-order modulations, but these are not typically examined as backgrounds. It appears that the statistic is most effective at detecting quadrupole ($l = 2$) modulation; even so, it unfortunately requires a very high modulation amplitude of $A \approx 0.8 - 0.9$ to obtain a 3-sigma result.

### E.   Multiple multipole modulation

We next investigate a variation of our multipole modulation approach, by applying a modulation across multiple multipoles.

$$T_{\text{new}}(\hat{\Omega}) = T_{\text{old}}(\hat{\Omega})[1 + A(\hat{\Omega} \cdot \hat{n})]^{l_{max}} \tag{IV.8}$$

$$= T_{\text{old}}(\hat{\Omega}) \left[ 1 + \sum_{l=1}^{l_{max}} \binom{l_{max}}{l} (A\hat{\Omega} \cdot \hat{n})^l \right] \tag{IV.9}$$

Here, $l_{max}$ is a constant denoting the highest order of our tongue-twisting 'multiple multipole modulation', which applies a series of modulations up to order $l_{max}$. Thus, keeping the statistic defined above, we seek to vary $l_{max}$ and the modulation amplitude $A$ to determine if it is possible to detect small signals for higher orders of modulation with the multipole statistic we have previously defined.

The results are more encouraging, as shown in Figure 13. For higher order modulations, such as $l = 10$, we are able to considerably reduce the amplitude required to obtain a $3\sigma$ result to $A \approx 0.2$. Unfortunately, this is still rather high compared to fiducial amplitudes, but it is a vast improvement from the previous result.

### F.    Issues for further consideration with multipole vectors

There are several major issues which must be considered for further development of this path of inquiry.

First is the selection of a statistic. Ours (Eq IV.6) was chosen for simplicity, but there may be far superior methods for detecting multipole modulation. However, our statistic also has the advantage of being a general one which detects correlation with a specific direction, rather than a specific signal - utilizing several such specialized statistics would run into issues with *a priori* statistics. It may, however, prove useful to weigh the statistic with the $A^{(l)}$ scalars from Eq IV.3

Second is to develop a method for detection of best-fit correlation direction. Obviously, this can be done through computing our statistic for various directions in the random sky and selecting the direction which maximizes it, but this is a very time-inefficient method. As is, without such a method, our statistics are incomplete and overly optimistic, and we are restricted to working with injecting backgrounds into random skies, where we will know the correlation direction.

An additional less significant issue is the lack of a mask in our analysis. This is due to the complex calculations required to reconstruct the $a_{lm}$s in a masked sky - although we have code to perform this task, it takes a considerable amount of time even at low resolution values. Reconstructing the $a_{lm}$s of 10,000 random skies at $N_{\text{side}} = 16$ would require $\approx 2\frac{1}{3}$ days of valuable computational time, not to mention the time required to decompose the $a_{lm}$s into multipole vectors. Unfortunately, time simply did not permit us to account for masked skies.

It should also be considered if attempting to detect multipole modulation is the best use for multipole vectors - it may be that multipole vectors are better suited for detection of other types of signals.

## V.    CONCLUSION

Our results are somewhat disappointing; it transpire that the techniques used within this study require considerably large signals before detection at $3\sigma$ is possible. However, it is still useful to examine the topic. This work will assist us in refining search techniques for future study. It is also useful to know how to test the sensitivity of one's search techniques. Though this study consists mostly of negative results, it could at the least be useful in alerting others of which venues of study *not* to pursue.

## VI.    ACKNOWLEDGEMENTS

students in the future.

For the results in this paper, we acknowledge use of the HEALPix [31] package, and also the Legacy Archive for Microwave Background Data Analysis (LAMBDA). We also acknowledge the use of multipole vector decomposition code, written by Craig Copi [6].

[1] A. A. Penzias and R. W. Wilson, Astrophys. J. **142**, 419 (1965).

[2] C. L. Bennett *et al.* (WMAP), Astrophys. J. Suppl. **148**, 1 (2003), arXiv:astro-ph/0302207.

[3] D. N. Spergel *et al.* (WMAP), Astrophys. J. Suppl. **170**, 377 (2007), arXiv:astro-ph/0603449.

[4] G. Hinshaw *et al.* (WMAP), Astrophys. J. Suppl. **180**, 225 (2009), arXiv:0803.0732 [astro-ph].

[5] N. Jarosik, C. L. Bennett, J. Dunkley, B. Gold, M. R. Greason, M. Halpern, R. S. Hill, G. Hinshaw, A. Kogut, E. Komatsu, D. Larson, M. Limon, S. S. Meyer, M. R. Nolta, N. Odegard, L. Page, K. M. Smith, D. N. Spergel, G. S. Tucker, J. L. Weiland, E. Wollack, and E. L. Wright, Astrophys. J. Suppl. **192**, 14 (2011), arXiv:1001.4744 [astro-ph.CO].

[6] K. Land and J. Magueijo, Phys. Rev. Lett. **95**, 071301 (2005).

[7] J. Hoftuft, H. K. Eriksen, A. J. Banday, K. M. Górski, F. K. Hansen, and P. B. Lilje, Astrophys. J. **699**, 985 (2009), arXiv:0903.1229 [astro-ph.CO].

[8] F. K. Hansen, A. J. Banday, K. M. Gorski, H. K. Eriksen, and P. B. Lilje, Astrophys. J. **704**, 1448 (2009), arXiv:0812.3795 [astro-ph].

[9] J. Kim and P. Naselsky, Phys. Rev. **D82**, 063002 (2010), arXiv:1002.0148 [astro-ph.CO].

[10] M. Cruz, E. Martinez-Gonzalez, P. Vielva, and L. Cayón, MNRAS **356**, 29 (2005), astro-ph/0405341.

[11] M. Cruz, M. Tucci, E. Martinez-Gonzalez, and P. Vielva, Mon. Not. Roy. Astron. Soc. **369**, 57 (2006), arXiv:astro-ph/0601427.

[12] M. Cruz, L. Cayon, E. Martinez-Gonzalez, P. Vielva, and J. Jin, Astrophys. J. **655**, 11 (2007), astro-ph/0603859.

[13] Zhang and Huterer, Astroparticle Physics **33**, 69 (2010), arXiv:0908.3988 [astro-ph.CO].

[14] I. J. O'Dwyer, H. K. Eriksen, B. D. Wandelt, J. B. Jewell, D. L. Larson, K. M. Górski, A. J. Banday, S. Levin, and P. B. Lilje, The Astrophysical Journal Letters **617**, L99 (2004), arXiv:astro-ph/0407027.

[15] D. N. Spergel *et al.* (WMAP), Astrophys. J. Suppl. **148**, 175 (2003), astro-ph/0302209.

[16] C. J. Copi, D. Huterer, D. J. Schwarz, and G. D. Starkman, Mon. Not. Roy. Astron. Soc. **367**, 79 (2006), astro-ph/0508047.

[17] C. J. Copi, D. Huterer, D. J. Schwarz, and G. D. Starkman, Phys. Rev. D **75**, 023507 (2007), arXiv:astro-ph/0605135.

[18] C. J. Copi, D. Huterer, D. J. Schwarz, and G. D. Starkman, Mon. Not. Roy. Astron. Soc. **399**, 295 (2009), arXiv:0808.3767.

[19] A. Pontzen and H. V. Peiris, Phys. Rev. D **81**, 103008 (2010).

[20] S. Zhang, The Astrophysical Journal Letters **748**, L20 (2012), arXiv:1109.6936 [astro-ph.CO].

[21] K. Land and J. Magueijo, Mon. Not. Roy. Astron. Soc. **362**, 838 (2005), astro-ph/0502574.

[22] D. Huterer, New Astron. Rev. **50**, 868 (2006), astro-ph/0608318.

[23] C. L. Bennett, R. S. Hill, G. Hinshaw, D. Larson, K. M. Smith, J. Dunkley, B. Gold, M. Halpern, N. Jarosik, A. Kogut, E. Komatsu, M. Limon, S. S. Meyer, M. R. Nolta, N. Odegard, L. Page, D. N. Spergel, G. S. Tucker, J. L. Weiland, E. Wollack, and E. L. Wright, Astrophys. J. Suppl. **192**, 17 (2011), arXiv:1001.4758 [astro-ph.CO].

[24] L. Cayon *et al.*, Mon. Not. Roy. Astron. Soc. **326**, 1243 (2001), arXiv:astro-ph/0105111.

[25] E. Martinez-Gonzalez, J. E. Gallegos, F. Argueso, L. Cayon, and J. L. Sanz, Mon. Not. Roy. Astron. Soc. **336**, 22 (2002), arXiv:astro-ph/0111284.

[26] C. Copi, D. Huterer, and G. Starkman, Phys. Rev. **D70**, 043515 (2004), arXiv:astro-ph/0310511.

[27] D. J. Schwarz, G. D. Starkman, D. Huterer, and C. J. Copi, Phys. Rev. Lett. **93**, 221301 (2004), astro-ph/0403353.

[28] D. Hanson and A. Lewis, Phys. Rev. D **80**, 063004 (2009).

[29] H. K. Eriksen, F. K. Hansen, A. J. Banday, K. M. Górski, and P. B. Lilje, Astrophys. J. **605**, 14 (2004), astro-ph/0307507.

[30] H. K. Eriksen, A. J. Banday, K. M. Górski, F. K. Hansen, and P. B. Lilje, The Astrophysical Journal Letters **660**, L81 (2007), arXiv:astro-ph/0701089.

[31] K. M. Górski, E. Hivon, A. J. Banday, B. D. Wandelt, F. K. Hansen, M. Reinecke, and M. Bartelmann, Astrophys. J. **622**, 759 (2005).

---

[6]Downloaded from his website, http://www.phys.cwru.edu/projects/mpvectors